

# Local and Global Granular Mechanical Characteristics of Grain–Structure Interactions

Z. K. Jahanger<sup>1,2</sup> · J. Sujatha<sup>3</sup> · S. J. Antony<sup>1</sup> 

Received: 24 June 2017 / Accepted: 5 January 2018 / Published online: 15 January 2018  
© Indian Geotechnical Society 2018

**Abstract** The focus of this work is on systematically understanding the effects of packing density of the sand grains on both the internal and bulk mechanical properties for strip footing interacting with granular soil. The studies are based on particle image velocimetry (PIV) method, coupled with a high resolution imaging camera. This provides valuable new insights on the evolution of slip planes at grain-scale under different fractions of the ultimate load. Furthermore, the PIV based results are compared with finite element method simulations in which the experimentally characterised parameters and constitutive behaviour are fed as an input, and a good level of agreements are obtained. The reported results would serve to the practicing engineers, researchers and graduate students in unravelling the mechanics of granular soil at both local and global levels when they interact with structures. The outcomes would be beneficial not only to the geotechnical engineering community, but also to related disciplines

dealing with granular materials such as materials processing, minerals and space exploration.

**Keywords** Granular mechanics · PIV · FEM · Bearing capacity · Grain–structure interaction

## Introduction

Cohesionless sands comprise of discrete grains of varying size and packing density. Their mechanical behaviour is different from that of conventional solid, liquid and gaseous state of matter [1]. Numerous researchers have studied the micromechanical characteristics of granular materials using experiments, theoretical descriptions and computer simulations [2]. From the micromechanical perspective [3], some studies have attributed the origin of shear strength of granular media to the anisotropy of strong force chains [4–6]. Their dilation characteristics are attributed to the displacement network of granular media [7].

In foundation engineering, ultimate bearing capacity ( $q_{ult}$ ) and allowable settlement ( $S$ ) are used as key design parameters [8, 9]. In sand, settlement controls the design criteria of footing [10, 11] which is independent of the loading rate [9]. Also, the settlement of footings could depend on their width for a given soil [11], but ultimate bearing capacity of sand is less dependent on footing width ( $B$ ) when less than 1 m as reported by Terzaghi and Peck [12]. In soil–structure interaction analysis [13], engineers use constant vertical displacement profiles for rigid footings interacting with sand at the level of the footing. However, the settlement in sand could vary significantly below the level of the footing–sand interface within the influence zone of depth ( $z$ ) about 2–4 times the width of the footing ( $B$ ) in homogenous sand [14, 15]. The previous

**Electronic supplementary material** The online version of this article (<https://doi.org/10.1007/s40098-018-0295-5>) contains supplementary material, which is available to authorized users.

✉ S. J. Antony  
S.J.Antony@leeds.ac.uk

Z. K. Jahanger  
ml13zkj@leeds.ac.uk; zuhairkadhim@gmail.com

J. Sujatha  
judessuja@yahoo.com

<sup>1</sup> School of Chemical and Process Engineering, University of Leeds, Leeds LS2 9JT, UK

<sup>2</sup> Department of Water Resources Eng, College of Engineering, University of Baghdad, Al-Jadriya Campus, Baghdad, Iraq

<sup>3</sup> Department of Civil Engineering, University College of Engineering, Nagercoil, India

research discussed above on the settlement profiles along the footing central axis do not vary linearly with depth. However, detailed information on how the displacement field evolves within the sand bed under mechanical loading is still not well established. Historically, bi-linear model (simple triangle approximation) is used to describe the variation of elastic displacement in sands [14] and others use nonlinear variation [16]. At the micro scale, grain displacements are non-uniform [17]. However experimental results on the role of relative density of sand for all three major types, loose, medium-dense and dense sand on their geomechanical characteristics using particle image velocimetry (PIV) is not yet probed systematically. This is addressed here using two-dimensional particle image velocimetry (PIV). The Dynamic Studio Software Platform (DSSP) helps to display the large amounts of PIV-based experimental data in pictorial forms [18]. Recently PIV was applied to understand the flow properties of granular materials [19]. Here, the authors focus on the local deformation and velocity fields and bulk strength for different relative densities of sand when a strip shallow footing interacts with sand under quasi-static axial loading ( $P$ ). Detailed experimental characterisation of the sand material is made using a range of experiments. The aim is at first to compare the variation of displacement fields measured in sand packing using PIV with FEM analysis. Thereafter, the variation of fundamental mechanical features at both local and global scales are studied in detail using PIV for strip footing interacting with sand packing of different relative densities in a systematic manner.

### Digital Particle Image Velocimetry (DPIV) Analysis

DPIV pertains to the digital platform of Particle Image Velocimetry (PIV), is often used in the field of fluid mechanics to track the motion of fluid flow using tracer particles [20]. It has been also used to study the displacement and/or strain distribution in some cases of granular materials [21, 22]. Recently, PIV has been applied to get measurements of soil deformation in geotechnical engineering problems [21–25]. In this study, DSSP is used to analyse the digital images acquired during test using PIV. The DSSP platform provides a range of techniques for characterising particle motions, making it the most convenient for making advanced scientific imaging-based measurements [18]. The algorithms provided within DSSP are used to analyse the PIV measurements further. This functionality built in the DSSP was used to analyse the digital frames of the grains, and to calculate two velocity components vectors of the grains and their evolution during load application within the sand layer between two

successive images. In this study, the area of interest or the target area (full image) was specified before being divided into sub-sections called interrogation areas (IA) of  $16 \times 16$  pixels each covering a zone of soil approximately  $2.2 \text{ mm}^2$ . Each of these interrogation area was tracked using an adaptive PIV method [18, 19, 26] to identify the movement of soil based on particle images (here 30 images per second) obtained from the front of the Perspex test rig. The interrogation areas from each successive images are cross-correlated with each other, pixel by pixel [18]. The correlation produces a peak signal detection, identifying the common grains movement and thus also the velocity vector output is computed with sub-pixel interpolation. A velocity vector plot over field of view (target area) is acquired by repeating the cross-correlation for each interrogation area over the two images [18].

### Materials and Experiments

The samples used here are disturbed dry silica sand samples obtained in UK. Sand properties were characterised (Table 1) according to the American Society for Testing and Materials [27, 28]. Their experimentally measured material properties and size distribution showed the following properties: maximum dry density ( $\gamma_{d \text{ max.}}$ ) =  $16.50 \text{ kN/m}^3$  and minimum dry density ( $\gamma_{d \text{ min.}}$ ) =  $14.23 \text{ kN/m}^3$ . In addition, using the sieve analysis as shown in Online Resource OR1, the following properties of sand were obtained from the grain size distribution curve:  $D_{10} = 0.25 \text{ mm}$ ;  $D_{30} = 0.31 \text{ mm}$ ;  $D_{60} = 0.40 \text{ mm}$  (10, 30 and 60% of the particles are finer than these particular particle sizes respectively);  $D_{50} = 0.37$  (Mean grain size of soil particle); uniformity coefficient  $C_U = 1.55$ ; and the coefficient of curvature  $C_C = 0.93$ . These data revealed that the soil chosen is a poorly graded sand [17, 29]. The roundness of the grain was mostly spherical to sub-prismoidal and the angularity of the grains are characterised as angular and sub-angular [28]. For this, digital microscopy images of the grain samples were used as shown in the Online Resource OR1.

Bearing capacity of the footing was tested using an aluminium box of 460 mm in length, 300 mm in height and 39 mm in thickness, filled with dry silica sand. The box had smooth and transparent Perspex walls of 15 mm thickness also to eliminate any bending effects during the test (Fig. 1). The authors also verified during all tests that under the ultimate loads ( $P_{\text{ult}}$ ) of the dense sand packing did not lead to any remarkable out of plane movement of the container's face. This was checked using a dial gauge (0.01 mm resolution) mounted to the side walls from a magnetic base (though the picture of this arrangement is not included here). The surface roughness of the footing in

**Table 1** Experimentally measured physical properties of the sand used

Type of sand	Loose (L)	Medium-dense (M)	Dense (D)	Standards
Dry density, $\gamma_d$ (kN/m <sup>3</sup> )	14.70	15.30	15.80	ASTM C29/C29M
Void ratio, $e_o$	0.76	0.70	0.64	
Relative density, $D_r$ (%)	24	53	72	ASTM C128
Peak angle of internal friction, $\phi_{peak}$ (°)	32 (32.4)*	39 (39.5)*	44.3 (46.1)*	ASTM D3080
Residual angle of internal friction, $\phi_{cr}$ (°)	30	32	36.3	
Maximum dry density, $\gamma_{dmax}$ (kN/m <sup>3</sup> )	16.50			ASTM D698
Minimum dry density, $\gamma_{dmin}$ (kN/m <sup>3</sup> )	14.23			ASTM D4254 method C
Maximum void ratio, $e_{max}$	0.83			ASTM C29/C29M
Minimum void ratio, $e_{min}$	0.58			ASTM C29/C29M
$D_{10}$ (mm)	0.25			
$D_{30}$ (mm)	0.31			ASTM D421
$D_{50}$ (mm)	0.37			ASTM D422
$D_{60}$ (mm)	0.40			
Uniformity coefficient, $C_U$	1.55			ASTM D2487
Coefficient of curvature, $C_C$	0.93			
Mineralogy	Silica			Head (2006)
Grain shape	Mostly spherical			
Angularity of grains	Angular and sub angular 34°			Head (2006)
Angle of repose of the sand				

(\*) Direct shear test results

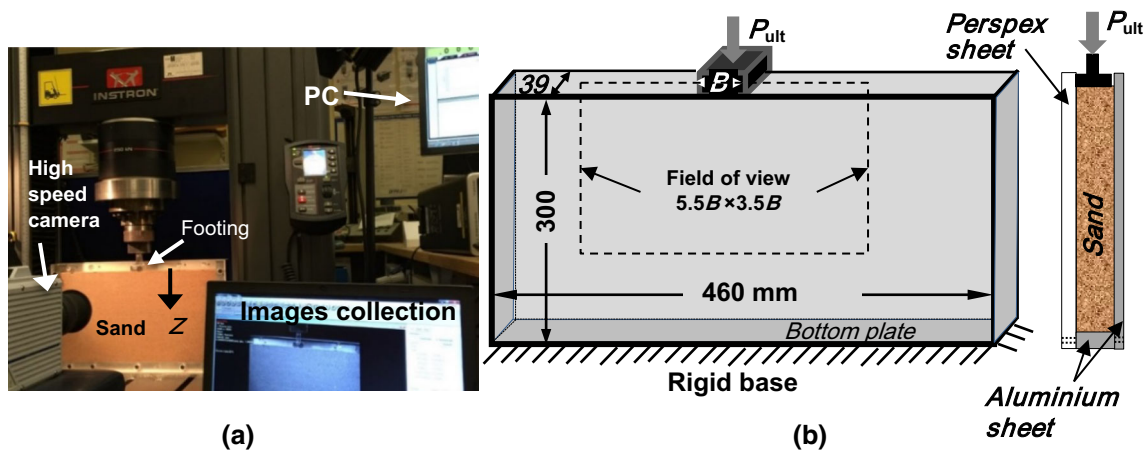


**Fig. 1** **a** Experimental setup using PIV with a live image of footing in contact with sand, **b** schematic diagram of the experimental setup (dimensions are in mm)

contact with sand, and the Perspex walls of the experimental box was measured using 3D optical microscopy based on white light interferometry [30] from which the mean roughness value  $R_a$  was obtained as 3.204 and 0.99  $\mu\text{m}$  respectively. The rigid foundation base was relatively rough [ratio between the angle of interfacial friction of the footing ( $\delta$ ) and angle of internal friction of the sand ( $\phi$ ), ( $\delta/\phi$ ) is 0.25]. Two cases of footing width are considered in this study, i.e., smaller and larger footing width with dimensions  $38 \times 38 \times 15 \text{ mm}^3$  and

$76 \times 38 \times 15 \text{ mm}^3$  respectively (footing width  $B/D_{50} = 102$  and 204 respectively to avoid any grain size effect, and height = 15 mm) was used here. It is recognised that the scale effects of the footing model could affect the estimations of their strength characteristics [31]. For example, a footing with relatively small width would require a relatively low stress level in the laboratory experiments, as if it were on a denser “state” of soil than a larger footing, even if they were tested on sand with the same void ratio [31]. To minimize the scaling effect, it is

suggested that the model testing for studying the effect of packing density should not be too close to the limits of void ratio ( $e_{\max}$  and  $e_{\min}$ , [32]). Taking this into account in the present study, the packing densities are kept away from these limits (Table 1). The value of  $B/D_{50}$  used here is within the permissible limit of testing strip footing in the lab although footing sizes used in real practice could be higher [33]. Such model dimensions have been used in previous experimental studies in this field [8, 34]. To minimise any frictional effects of the footing with the wall, a small gap of 1 mm is allowed between the footing and the back wall, so that they do not affect the deformation of the soil recorded by PIV at the front of the box. It is also worth noting that about 12.5% of particles were in the size range of 0.5–0.9 mm as shown in the Online Resource OR1, which helped to avoid any noticeable leakage of grains from behind the footing. These measures ensure that the observed movement from the images is due to the inner movement in the grains under mechanical loading [30].

The degree of compaction of granular soil is normally characterised according to the relative density  $D_r$ , defined as [35]:

$$D_r(\%) = \frac{e_{\max} - e}{e_{\max} - e_{\min}} \times 100 \quad (1)$$

where  $e_{\max}$  and  $e_{\min}$  are void ratio of the soil in loosest and densest conditions respectively and  $e$  is in-place void ratio of the tested soil (Table 1). Three cases of relative densities ( $D_r$ ) loose (L), medium-dense (M) and dense (D) were used in this study. The loose granular packing ( $\gamma = 14.7 \text{ kN/m}^3$ ,  $D_r = 24 \pm 2\%$ ,  $e = 0.76$ ) was prepared by pouring the grains mass uniformly across the width of the box in small layers using pluviation technique method [36] so that any segregation of the grains was avoided during the construction process. The top surface of the sand layer was gently levelled off using a hand scraper. This researchers also took care not to disturb the constructed loose sample in any way before applying the axial loading in our experiments. The mass of sand grains laid in the box to the required height pertains to the density of the loose sample. The medium-dense packing ( $\gamma = 15.30 \text{ kN/m}^3$ ,  $D_r = 53 \pm 2\%$ ,  $e = 0.7$ ) was hand compacted in three layers, using 50 blows per layer in 0.035 m lifts each with a  $16 \text{ cm}^2$  compaction hammer of 0.92 kg weight designed for this purpose [31]. The dense sand ( $\gamma = 15.80 \text{ kN/m}^3$ ,  $D_r = 72 \pm 2\%$ ,  $e = 0.64$ ) was achieved in five layers, 60 blows per layer. The footing was placed symmetrically on the top surface of the sand bed.

An axial compression loading ( $q$ ) was applied slowly on the footing (0.05 mm/s penetration velocity) using an Instron loading machine with 0.1 N resolution (Fig. 1). The loading machine also had an inbuilt dial gauge (linear variable differential transformer, LVDT) to record the

vertical displacement of the indenting footing on the sand packing. The macroscopic load and vertical displacement of the footing were also measured from the tests. The PIV camera with an allowable frame speed up to 100,000 frames per second (fps) was fixed in front of the box and two light sources were used to illuminate the rig. However, as the loading condition is quasi-static in this study, the recording at 30 fps was found to be adequate until soil failure was reached, although higher frame speeds were considered in the early stages of the experimental programme. We had verified that the recording at greater than 30 fps did not affect the result noticeably. The resolution of the images was  $1920 \times 1080$  pixels. Initially, a number of trials were conducted to determine the suitable acquisition rate of the recorded PIV images for the analysis. It was found that, for the current experiments, an acquisition of 1 frame/s of the recoded images is adequate in which images were captured at displacement increments of 0.0017 mm. DSSP was used to analyse the images using an adaptive PIV [18]. The adaptive PIV iteratively adjust the size of the individual interrogation areas (IA) in order to adapt to local seeding densities and flow gradients [18]. This is suitable to study granular systems even under different flow conditions [19] and bearing capacity of layered system [26]. Here, the distribution of velocity vectors of the grains was examined in the image analysis using a minimum interrogation area (IA) of size  $16 \times 16$  pixels and maximum IA size of  $64 \times 64$  with a measurement resolution of sub-pixel [18]. The space-pixel dimension of the measurement was calibrated by printing a known scale on the test box along the horizontal and vertical directions. White et al. [24] have shown that the precision of the measurement (i.e., the random difference between multiple measurements of the same quantity) improves with larger PIV patches and it is inversely proportional to the amount of the measurement resolution. This size of the mesh patch used here reveals a standard error better than 0.01 pixel [18, 24]. In the experiments, two illumination lights were positioned above the testing box to avoid reflection and glare on the measurement side of the Perspex wall. It was verified that the variation in image scale in both horizontal and vertical direction were not significantly different. The PIV camera lens was focused normal to plane the footing–soil interface region where the measurements are most important to make. Therefore, the dimension of target area was  $\sim 5.5B \times 3.5B$  (Fig. 1). The displacement measures i.e. resultant displacement ( $S_R$ ), vertical displacement ( $S_V$ ) and horizontal displacement ( $S_H$ ) were evaluated under a given load in total (i.e., between the reference image at zero load ( $q = 0$ ) and the image at the required fractions of the ultimate load level, such as  $0.34q_{\text{ult}}$  and  $q_{\text{ult}}$ . A typical mean size of sand grain ( $D_{50} = 0.37 \text{ mm}$ ) was represented

by about  $3 \times 3$  pixels. Hence the PIV experimental measurements made here are at the local-scale.

Following the footing tests, two standard cone penetration test (CPTs) tests were also conducted for each soil density to characterise the samples using a 10 mm diameter model CPT [25, 29]. The CPT was inserted at a penetration rate of 1 mm/s in the current experiments as shown in Online Resource OR2, but using the identical filling procedure of the grains used in the footing–sand indentation experiments presented earlier. Figure 2 shows the CPT penetration profiles for the soil for all sand packings. The penetration resistance (cone resistance =  $q_c$ ) profiles are plotted against the penetration depth from the bottom level of the footing.

As expected, the penetration resistance of dense sand is higher than medium-dense and loose sand. The penetration resistance of loose sand remains almost constant with depth after  $z/B = 2.5$ , but penetration resistance for medium-dense and dense sand increase with depth at an increasing rate. The rate of the penetration resistance of dense sand is larger than that of the medium-dense. Again, the differences in the penetration resistance for different relative densities are primarily accounted for the relatively larger volumetric compressibility in loose, medium-dense sand than the dense sand. The CPTs results for all the densities show the average response of the two results (error within 5%).

## FEM Simulations

Non-linear elastic finite element simulations have been made for the cases of a single footing indenting on the loose, medium-dense and dense sand packing using ANSYS workbench 17.2 version [37]. The ANSYS

program is a broad purpose finite element modelling (FEM) package for numerically solving a wide variety of mechanical interactions [37].

In the present study, ANSYS is used to create a two-dimensional solid geometry. The chosen domain along with applied boundary conditions is shown in Fig. 3. The simulations were held under identical boundary conditions for footing indenting with different types of sand packing as in the case of physical experiments. In the simulations, the bottom most nodes were fully constrained in both the horizontal and vertical directions ( $S_v = S_h = 0$ ). A line of symmetry is used along the footing centre line ( $S_v \neq 0$ ,  $S_h = 0$ ). The far side of the assembly was fully constrained in the horizontal direction ( $S_h = 0$ ) and free to move in the vertical direction ( $S_v \neq 0$ ) [38, 39]. The contact regions between the rigid footing and the sand were modelled as a relatively rough surface (interface friction coefficient = 0.25) corresponding to the experimental study [40]. An adaptive FE mesh was generated at the footing–soil interface where the largest stresses and strains would be expected. It should be mentioned that Skewness mesh metric (a measure of mesh quality) of 0.132 maximum value was obtained which is acceptable [41]. The size of the elemental geometry is shown in Fig. 3. The nodes and element numbers in the soil body are equal to 44,000 and 14,360 respectively.

Material model for soil describes the nonlinear plasticity behaviour which depends on the engineering soil properties in the current ANSYS simulations. For this, the experimentally characterised bulk stress–strain relationship corresponding to the load–displacement curves of different packing densities presented in Fig. 4 are discretised into a large number of linear segments and fed as user defined digital input [37, 41].

Furthermore, the experimentally characterised material physical properties were used i.e. bulk density, initial modulus of elasticity ( $E$ ) and typical value of Poisson's ratio ( $\nu$ ) for sand ( $E = 25, 35$  and  $50$  MPa whereas  $\nu = 0.2, 0.25$  and  $0.35$  for the loose, medium-dense and dense sands respectively [11]). In the present analysis, ANSYS used the multilinear isotropic hardening of the stress–strain relation [41]. The width of the loading area is  $0.5B$ . The loading is applied vertically in increments of constant displacement of  $0.15B$ , uniformly across the width of the footing within the time step of  $0.01$  s ( $\sim 300$  cumulative iteration). The evolution of different displacement components in the solid geometry (depicting the sand packing) is tracked for different loading levels and compared with corresponding PIV measures later.

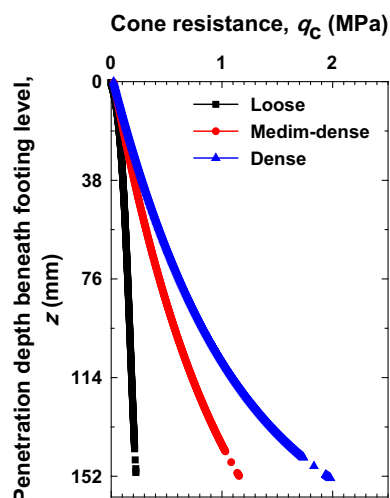
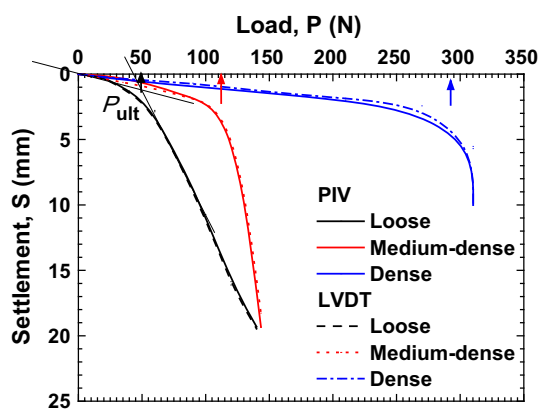
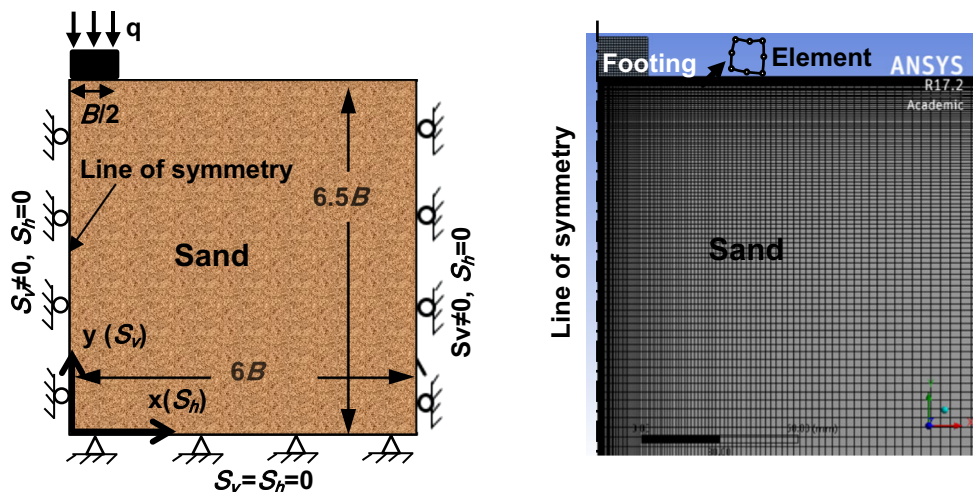


Fig. 2 CPT data for the sand packing

**Fig. 3** (left) Chosen domain and boundary conditions, half of domain analysis not to scale (right) finite element mesh, and element enlarged.  $S_v$  is vertical displacement component and  $S_h$  is horizontal displacement component.  $B$  is the footing width



**Fig. 4** Load–settlement curves of footing ( $B = 38$  mm) interacting with loose, medium-dense and dense sand. The guide arrows show the ultimate load level ( $P_{ult}$ ) of the sand packing

### Results and Discussions

The load–settlement relationship for a typical footing ( $B = 38$  mm) interacting with sand is presented in Fig. 4. It is worth mentioning that these PIV curves loads are simultaneously measured using the corresponding load outputs from the Instron. The settlements obtained using the PIV and LVDT gauge agree well. This justifies applying PIV to examine the displacement measures in sand layer later. Using the load–settlement data, the tangent intersection method [42] was applied to obtain the value of the ultimate bearing capacity (Fig. 4). The ratio of ultimate vertical settlement under ultimate load ( $S_u$ ) to footing breadth ( $B$ ),  $S_u/B$  is  $\sim 5.0, 7.1$  and  $11.7\%$  for the loose, medium-dense and dense sand respectively. These measures and the nature of bulk load–settlement curves are consistent [11] with punching (without a well-defined peak), local shear failure (moderate peak) and general shear failure (well-defined peak) for sand described by Liu and Iskander [17], Dijkstra et al. [29], Vesic [43].

Though not presented here, we also obtained a good level of comparison with De Beer’s study [44] for the variation of  $N_\gamma$  (Bearing capacity factor) with  $\gamma B$  for different sand packing. Both the bearing pressure and the failure strain increase with the packing density of sand. The authors wish to point out that, in the case of strip footings used in practice, 3D condition could exist around the ends of the strip footings even if the footing is long. However, for most parts of long strip footings, plane-strain condition could exist [8, 25, 30] as assumed in the current 2D plane-strain experiments [34].

The peak angle of internal resistance ( $\phi_{peak}$ ) for all cases of the packing density was also determined from triaxial compression test at different confining pressures 100, 200, and 300 kPa. For sands, the angle of internal friction typically ranges from  $26^\circ$  to  $45^\circ$ , increasing with the relative density. Three cases of relative densities were used as that in the experiment tests: loose, medium-dense and dense. The height of the sand samples was typically 76 mm, and the diameter was 38 mm. Subsequently, the plots of deviator stress ( $\sigma_d$ ) against axial strain ( $\epsilon_a$ ) were made. The peak angle of friction of the soil is obtained according to the stress state at peak strength. The measured angles of internal friction are  $32^\circ, 39^\circ$ , and  $44.4^\circ$  for loose, medium-dense and dense sand respectively. Using these, the peak angle of shearing resistance of the samples was evaluated and plotted against the relative density. This variation is described in (2) as:

$$\phi_{peak} = 24.7 + 0.267 D_r \tag{2}$$

Also the ( $\phi_{peak}$ ) determined from the standard direct shear test (ASTM D3080) under three different normal stresses 50, 100 and 200 kPa. The peak angle of shearing resistance of the samples was evaluated and plotted against the relative density. This variation is described in a mathematical form in (3) as follows:

$$\phi_{peak} = 25.2 + 0.277 D_r \quad (3)$$

This macroscopic relations obtained from the above said characterisation experiments are in agreement with other literature [8]. The authors wish to point out that, some literature suggest that the shear friction angle measured using direct shear tests may not pertain to that of sand under the plane strain experiments [36]. Jewell [45] suggested that symmetrical direct shear test could provide a more reliable measure of the plane strain angle of friction and the angle of dilation for sand than conventional direct shear test. In some studies, the angle of internal friction of sand obtained from the conventional direct shear test also correlated well with the experimental results of plane-strain condition [46]. However, in analysing the footing–soil interactions using theoretical and computational methods by idealising soil as an elastic media [47], friction angle does not form as a direct input in the analysis.

### Comparison of the PIV Measurements with FEM Analysis

Here the typical results are presented below for the case of footing interacting with the dense sand packing. Figure 5a, b shows the variation of PIV-based vertical displacement component and horizontal displacement component profiles in the dense sand at ultimate load and compared with the FEM (ANSYS) analysis. It is evident that a good level of agreement between the PIV and FEM approaches are obtained both qualitatively and quantitatively up to  $2.5B$  from the footing edges. Furthermore, quantitative comparison of variation of the normalised vertical displacement component  $S_v$ , and the normalised horizontal displacement component  $S_h$  along a horizontal section at a depth of  $0.5B$  below the level of footing under the ultimate load is provided for different packing conditions of sand in the Online Resource OR3. A good level of agreement is obtained between them. Figure 5c, d shows the variation of normal and shear elastic strain contours at ultimate load for the case of dense sand using FEM. It can be seen from the normal and shear elastic strain map that there is a strain concentration around the corner of the footing. It can be noticed from the contours of shear strain in the dense media that the soil is sheared in the area below the edge of the footing. Though not presented here, similar observations were made for the loose and medium-dense sand packing used in this study.

### PIV Based Analysis of Footing–Sand Interactions

Figures 6, 7 and 8 present typically the evolution of resultant velocity vectors in the sand packing under a typical load of  $q = q_{ult}$  ( $B = 38\text{mm}$ ). Also the

corresponding evolution of vertical and horizontal strain rate ( $\dot{\epsilon}_v$  and  $\dot{\epsilon}_h$  respectively) in the sand packing are provided which help to identify the difference regions of granular flow in the sand packing such as dead, active and passive zones as discussed below. The authors had also verified that these generic observations were similar in the case of the larger footing width ( $B = 76\text{ mm}$ ). A detailed evolution of this for three more stages of loading is provided in the Online Resource OR4–OR6. In this plot the contours of the vertical velocity are also obtained from the DSSP and superimposed for information.

At the early stages of the loading (c.a.  $q < 0.5q_{ult}$ ), approximately a triangular wedge of dead zone (region 1 in Figs. 6, 7 and 8 with a constant amount of resultant velocity of the grains but has the highest vertical velocity) is formed beneath the footing in all cases of packing densities [48]. The authors point out that the dead zone does not mean that the grains are not moving at all, but move as a block of grains with almost the same velocity. In granular mechanics, the dead-zone is characterised by the block of materials beneath the indenting objects with the granular materials, and moving as if they are continuous extension of the indenter, i.e., no slip at the indenter–granular interface [22]. Noticeably, outside this zone the particles tended to move downward and sideward symmetrically until the ultimate bearing capacity is reached in the sand packing. Similar trends were noticed in other studies, for example in sand [22], different soil types [48] and soft metal [49].

The depth of this wedge at the ultimate bearing load is equal to about  $B$ , whose vertices (slip planes) intersect the horizontal at an angle ( $\alpha = \text{Angle of dead zone wedge/active zone 1}$ ) of about  $62^\circ \pm 2^\circ$ . These are consistent with Prandtl's assumption [48] for smooth footing ( $\alpha = 45 + \phi/2$ ), which have not been confirmed using microscopic experiments, but using PIV here. Furthermore, Kumar and Kouzer [38] have reported similar measures for smooth footing using plasticity limit analysis with the help of finite element method (FEM). For a further increase in the load, the grains in the dead zone tend to punch the neighbouring grains in zone 2 radially outwards (Figs. 6, 7 and 8). A failure pattern consistent with Vesic [43] at the ultimate failure load is visualised (Figs. 6, 7 and 8, and as in Online Resource OR4–OR6) for all cases of sand considered here. By and large, the grains flow symmetrically with respect to the central axis of the footing until reaching the ultimate load ( $q = q_{ult}$ ) then, unsymmetrical flows occur beyond the ultimate load. This is consistent with the classical literature, e.g. Vesic [43] for medium and dense sand, but the current study observes that this could happen in the case of loose sand as well. At ultimate load, the dense soil failed suddenly corresponding to the pronounced peak in the bulk strength curve presented in Fig. 4, and the unsymmetrically strong velocity distribution presented in

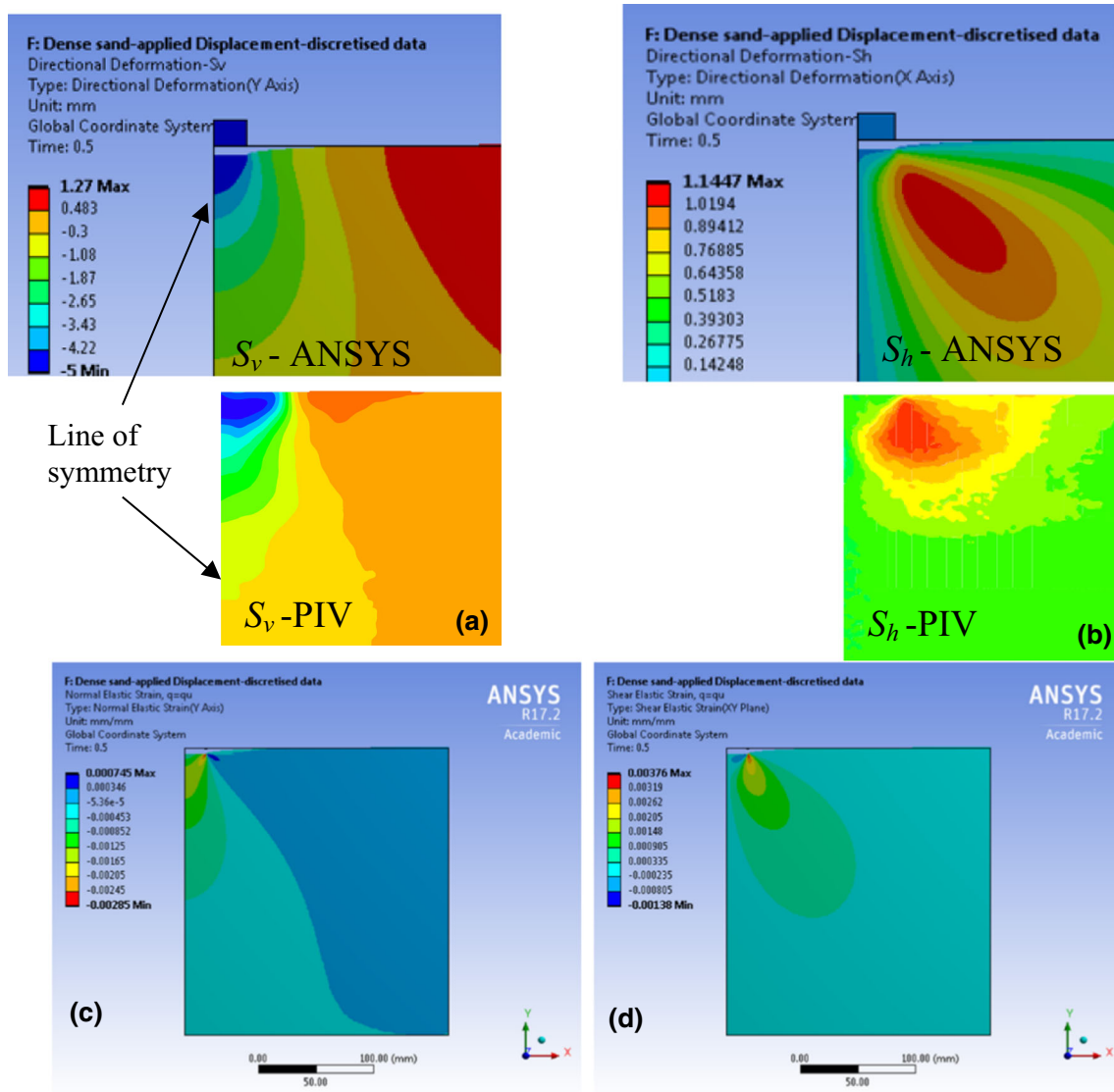


**Fig. 5** Comparison of PIV-based vertical displacement profile in dense sand at ultimate load below the footing with FEM analysis (identical colour codes are used): **a** vertical displacement component,

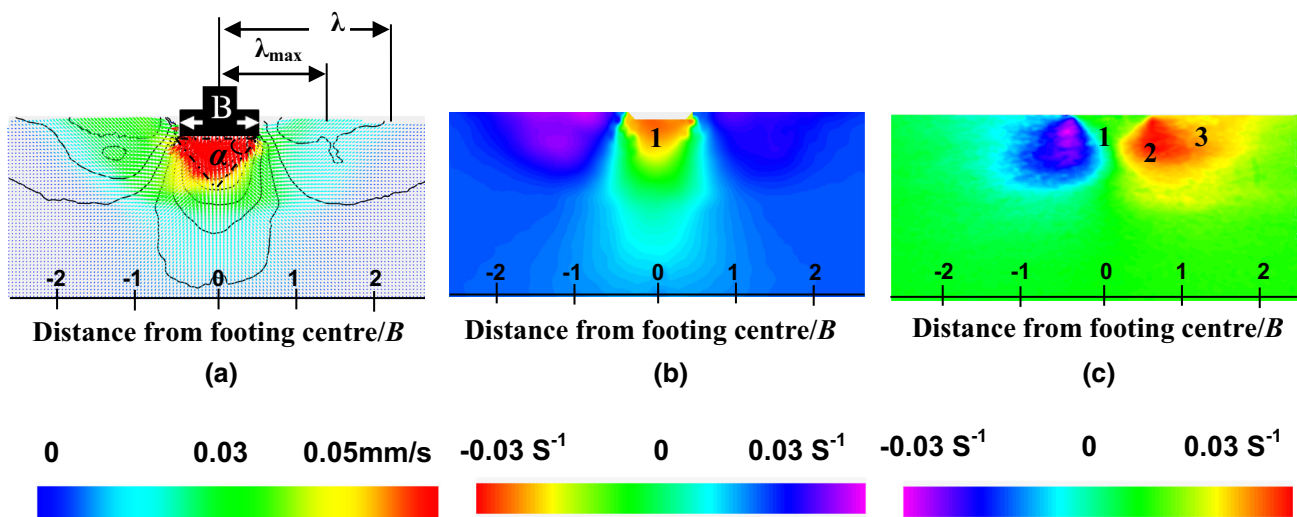
**b** horizontal displacement component below the footing. Taking advantage of FEM, the strain distributions are presented: **c** normal and **d** shear elastic strain

Fig. 8 at the localised level. So, in the higher relative density tests, the horizontal displacement (Fig. 8c) seems to be highly non-symmetric under ultimate load. In reality local structural non-homogeneities could exist, and this triggers the non-symmetrical flow of grain (post-failure) even under the symmetric loading conditions. At this stage, the grains flow like a fluid. The grains beneath this flow region are solid-like and almost stagnant. The shear failure occurs progressively from the dead zone and extending radially outwards.

The sand surface forms a heap spreading up to about  $2.7B$ ,  $2.6B$  and  $2.4B$  away from the footing centre ( $\lambda$  = Distance of sand heap from the centre of the footing, Fig. 6) for the loose, medium-dense and dense packing

respectively (Figs. 6, 7 and 8). The height of the heap attains maximum at distances of about  $1.7B$ ,  $1.55B$  and  $1.31B$  for loose, medium and dense sand respectively ( $\lambda_{\max}$  = location of sand heap attaining maximum height from the centre of the footing). The slope of sand heap at the ultimate load is  $31^\circ$ ,  $33^\circ$  and  $38^\circ$  for the loose, medium-dense and dense sand respectively. The average value of the slope of the heap for the different sand packing is  $(34^\circ)$  identical to the angle of repose of the sand. These angles are close to the residual angle of internal friction of the sand ( $\phi_{cr}$ ) about  $31^\circ$ ,  $33^\circ$ ,  $37^\circ$  for the loose, medium-dense and dense sand samples respectively. These residual angles are consistent with the previous literature [50].





**Fig. 6** a Resultant velocity vectors at a typical load of  $q = q_{ult}$  in loose sand and the scalar contours of the vertical velocity using PIV, b vertical strain rate  $\dot{\epsilon}_v$ , c horizontal strain rate  $\dot{\epsilon}_h$ . Zones: 1 dead zone, 2 active zone, 3 passive zone.  $B = 38$  mm

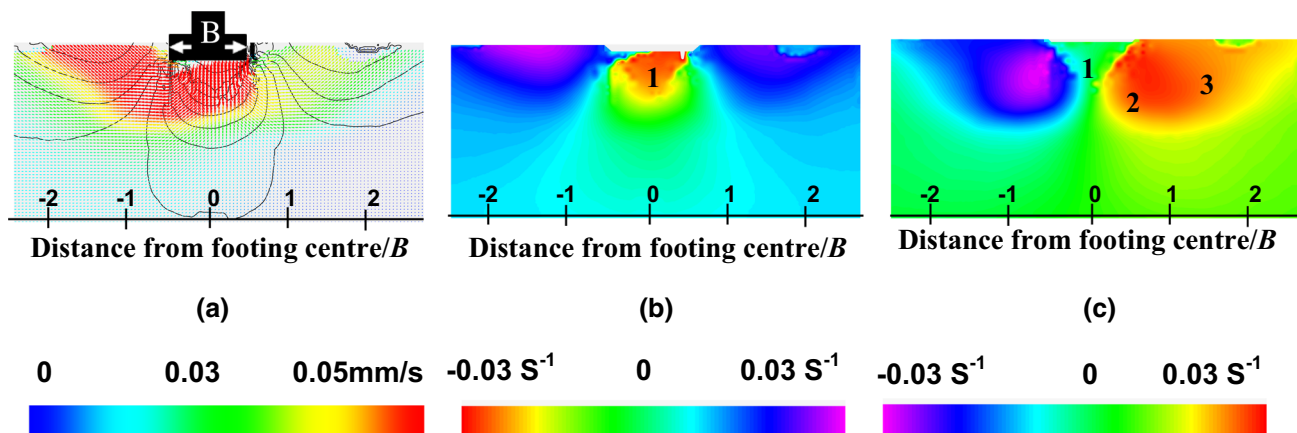


**Fig. 7** a Resultant velocity vectors at a typical load of  $q = q_{ult}$  in medium-dense sand and the scalar contours of the vertical velocity using PIV, b vertical strain rate  $\dot{\epsilon}_v$ , c horizontal strain rate  $\dot{\epsilon}_h$ . Zones: 1 dead zone, 2 active zone, 3 passive zone.  $B = 38$  mm

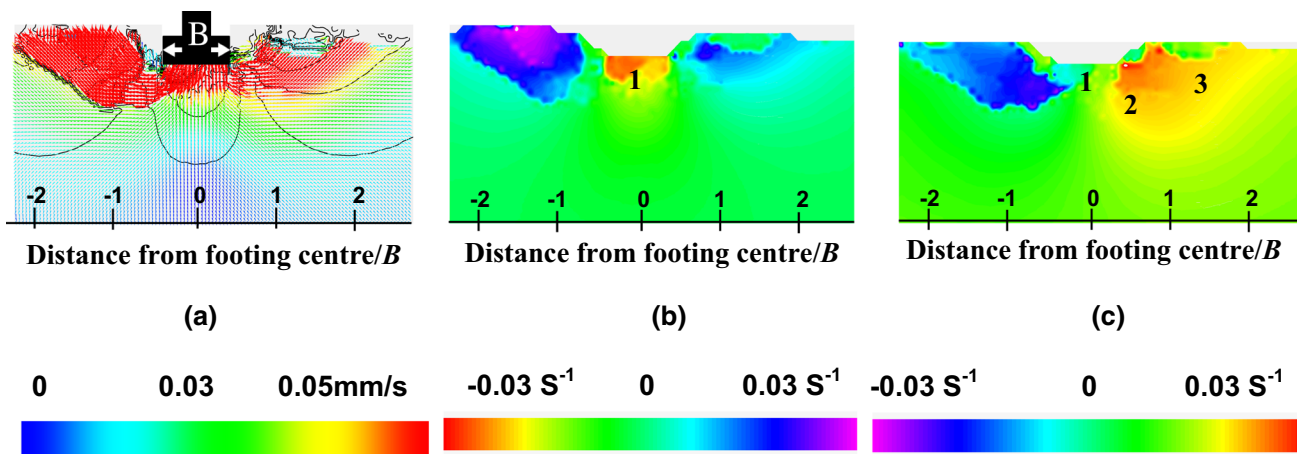


**Fig. 8** a Resultant velocity vectors at a typical load of  $q = q_{ult}$  in dense sand and the scalar contours of the vertical velocity using PIV, b vertical strain rate  $\dot{\epsilon}_v$ , c horizontal strain rate  $\dot{\epsilon}_h$ . Zones: 1 dead zone, 2 active zone, 3 passive zone.  $B = 38$  mm

The effect of sand packings at ultimate load on the failure mechanism are summarised both quantitatively and systematically in Fig. 9 for a typical case of footing ( $B = 38$  mm). This shows the resultant velocity vectors of soil movement at ultimate bearing capacity and the schematic diagram of the failure mechanism underneath the footing of different packing densities. It is evident that the footing load test in the loose packing corresponds to a punching failure and local shear mechanism, consistent with the literature [29]. On the other hand, tests in the medium-dense and dense packings exhibit a general failure mode with relatively larger horizontal displacement and soil heap next to the footing, typical of a conventional rigid plastic bearing capacity, and Prandtl's wedge-shaped zone mechanism [48]. Hence, the formations of velocity discontinuities are linked to the density of the sand packing.

Interestingly, the boundaries of the zone of plastic flow in sand at failure load sketched using PIV here (in terms of the resultant velocity vector, and the components of strain rate presented in Figs. 6, 7 and 8) are remarkably similar to such intuitive diagrams suggested by Fröhlich in the 1930s [48]. However, at or beyond the ultimate load, the PIV experiments have shown non-symmetric flow of grains even under the symmetric loading conditions on the footing. They could be attributed to the potential existence of (even minor level) non-symmetrical structural arrangements of the grains at local scale in reality. These could amplify the non-symmetrical velocity patterns under the above said condition.

Figure 10 shows the typical normalised vertical displacement component in dense sand at different horizontal

sections below the footing–soil interface under the ultimate load ( $q_{ult}$ ). The plots of this for loose and medium-dense sand are provided in the Online Resources OR7. It is evident that at a depth of  $z/B = 2.5$  the vertical displacement is practically negligible in all cases of footing width and packing densities. Furthermore, for a given packing density, the normalised vertical displacement in the soil at a given depth (e.g.  $z/B = 0.1$ ) decreases for an increase in the width of the footing under the ultimate load. However, here it is found that the absolute value of the vertical displacement in the soil for a given depth increases for increase in the width of the footing as also referred in other studies [51]. The heap close to the free surface (secondary peaks) increases with increasing relative density but decreases with  $z/B$  (Fig. 10). Also, the heap height decreases with footing width as shown in Online Resource OR7. This is related to potentially particles interlocking and rolling over of the grains. This has a significant effect in the development of the vortex map adjoining the footing sides [22]. The discontinuities in the velocity measures directly beneath the footing and the edges of the footing could result some error in the measurement [25]. However, these measurements are taken at and beyond a depth  $z/B = 0.1$  after the ultimate loading is applied. Therefore, any such potential errors are expected to be minimal here.

The images of flow of grains near the corner of the footing ( $B = 38$  mm) for a typical case of dense sand is superimposed on their resultant velocity distribution plots and presented in Fig. 11 for the pre-failure and post-failure stages. These plots for the cases of loose and medium-dense sand are provided in the Online Resource OR8. The grains

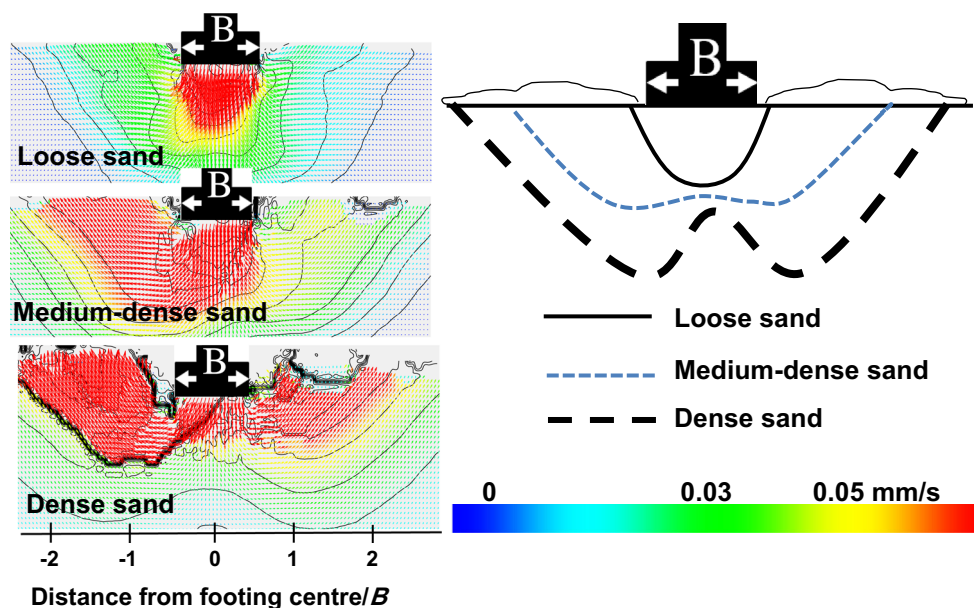


**Fig. 9** (left) Resultant velocity vectors of soil movement under ultimate bearing capacity,  $B = 38$  mm (right) sketch of general schematic failure mechanism underneath footing of different packing densities

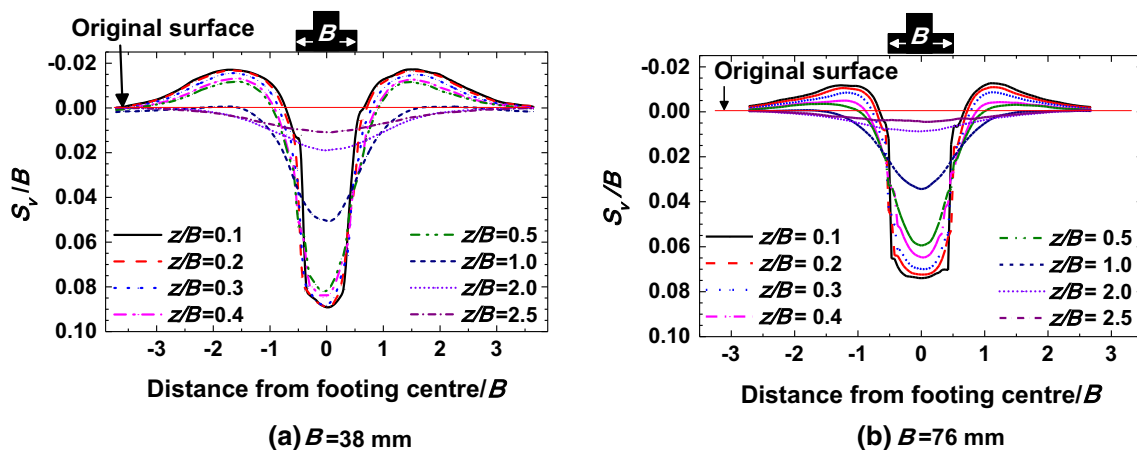


**Fig. 10** PIV-based normalised vertical displacement component profiles in dense sand under the ultimate load ( $q = q_{ult}$ ) along different horizontal sections at different depths ( $z/B$ ) from the footing–soil interface

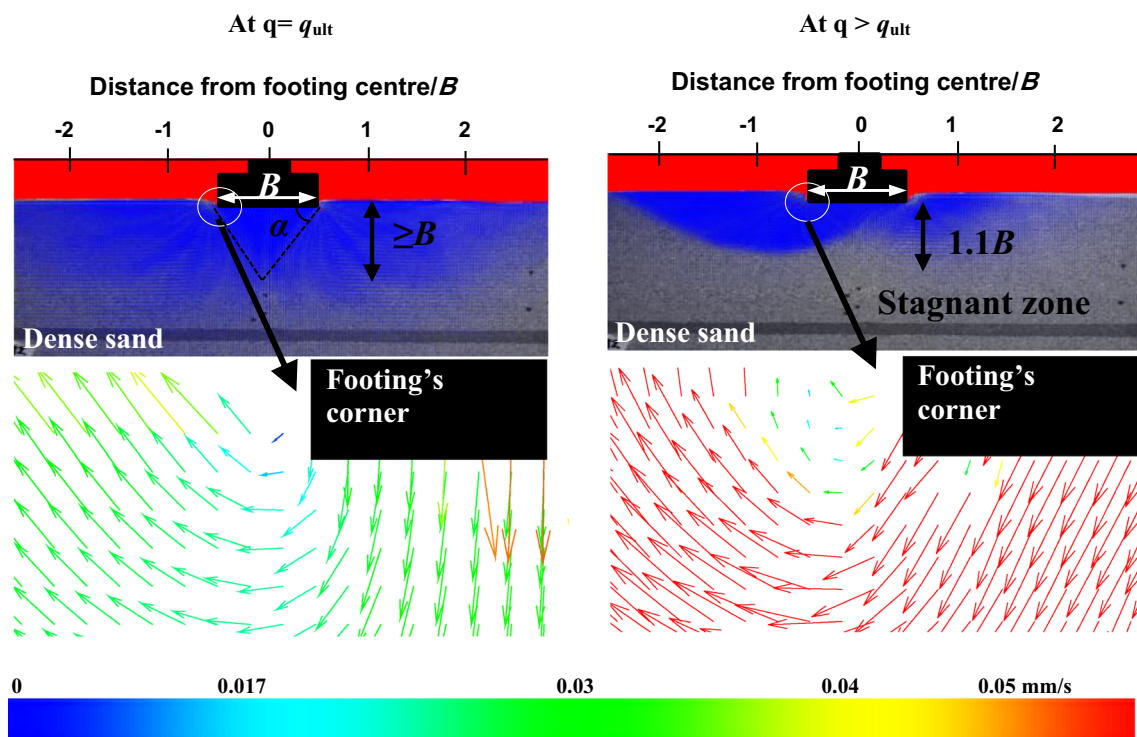


**Fig. 11** Vortex formation of resultant velocity vectors for footing ( $B = 38$ ) interacting with dense sand. Enlarged view of the corner of the footing is also presented here

flow radially outwards and non-uniformly in all cases of the sand packing. The grains resting beyond the influence zone of deformation (or velocity) do not move in the post-failure stage, which is beyond about  $1.25B$ ,  $1.2B$ , and  $1.1B$  for loose, medium dense and dense sand respectively for both cases of footing width. This trend is in agreement with Liu and Iskander [17] who stated that this influence zone is limited within a depth of about  $1B$  of the footing at post-failure stage in the case of loose sand ( $D_r$  is limited to 21% in their experiments). From the PIV results, the authors

observe that the depth of this influence zone is lower than that of pre-failure stages possibly due to relatively radially outwards movement from the edge of footing as a block, which is consistent with conventional Terzaghi’s bearing capacity analysis (Fig. 11) [48]. The vortex in the total velocity distribution profiles is clearly seen nearer the corner side of the footing for all sand densities. It started when the vertical displacement ( $S_v$ ) ratio  $S_v/B \sim 0.1$ . This is a result of gravitational movement of sand from the surface heap while the subsurface grains move upward with

loading. Eventually the grains fall back from the passive zone toward the edge of the footing and form a loop-like resultant velocity profile. The spatial nature of the vortex is consistent with Murthy et al. [22] where the sand medium was dense. The present study confirms the presence of such vortex maps in loose and medium-dense sand as well.

Computational studies based on finite element method, for example Griffiths et al. [52] and Kumar and Kouzer [38] have reported velocity discontinuities near the footing edge, but the current study has shown their evolution in the sand packing using PIV experiments. The presence of such vortices around the corner at  $q > q_{ult}$  is likely to be related to the local density at the corner rather than the bulk density underneath the footing. Hence, even in a loose sand under compression loading, once the materials close to the footing corner compact to a certain density that is close to the maximum density of the tested soil then vortex will be observed around the edge of the footing. Since features like this are really local features and not bulk features, so it is the density in the local zone around the corner that would be important than the whole soil density for characterise of the vortex formation.

Figure 12 quantifies the normalised vertical displacement component  $S_v$  and horizontal displacement component  $S_h$  of dense sand (for a typical case of  $B = 38$  mm) at different loading levels ( $q \leq q_{ult}$ ). These plots for loose and medium-dense sand are provided in the Online Resource OR9.  $S_v$  presents an inverted triangle-like profile that becomes deeper and narrower with increasing load level. The maximum value of  $S_v$  occurs along the footing centre, then decreases gradually towards the footing edge [17].  $S_v$  decreases to zero within a distance of  $0.25B$  from the footing edge. This behaviour is due to the lack of confinement in the soil [11]. The secondary peaks in the

distribution of  $S_v$  diminish with decrease in the density of sand. Such patterns, at times non-symmetric, are seen mostly at or beyond the ultimate load even under the symmetric loading conditions on the footing as discussed earlier. The secondary peaks increase with increasing density as shown in Online Resource OR9. This could be due to the particles interlocking, jamming and dilation that increase with the relative density of sand.

The profile of  $S_h$  component presents S-like shape with a neutral point (zero value) occurring along the axis of symmetry of the footing. The soil along the vertical axis of symmetry is confined by the maximum vertical displacement and therefore  $S_h \sim 0$ . It is worth mentioning that, though not presented here, the variation of resultant displacement ( $S_R = \sqrt{S_v^2 + S_h^2}$ ) at the footing–soil interface was uniform along the footing width.

Previous classical approaches have estimated the elastic settlement of footings using influence factors, which could vary along the depth of sand [8, 53]. Such variations are also observed from numerical solutions, for example using finite element method [53], elastic theory [16] and simple triangular profile using in situ cone penetration tests [14]. However, they show different types of profiles. Using PIV here, the variation of  $S_v/B$  along the centre line of the footing is examined, and  $S_h/B$  along the edge of the footing with depth for a typical case of dense sand ( $B = 38$  mm) is presented in Fig. 13. These results for the cases of loose and medium-dense sand are provided in the Online Resource OR10.

They show a nonlinear response for all cases of sand packing. They gradually decrease to a negligible value beyond  $\sim z/B = 2.5$ , similar results have been reported for loose sand by Liu and Iskander [17], however this distance decreases for an increase in the relative density of sand.

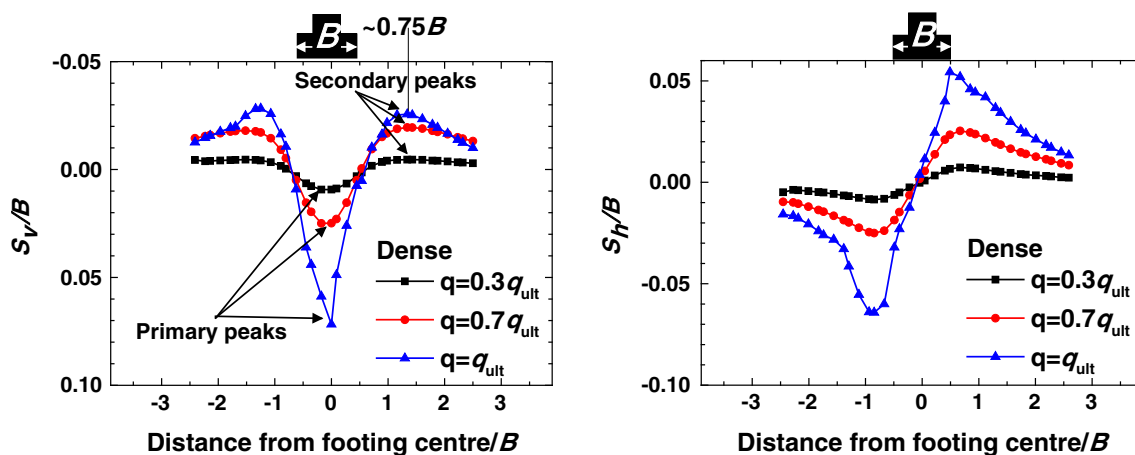


**Fig. 12** For a typical case of dense sand: (left) Normalised vertical displacement component (right) normalised horizontal displacement component at a horizontal cross section  $0.5B$  below footing using PIV at different loading levels. Signs: vertical displacement (positive

down, negative up), horizontal displacement (negative toward left, positive toward right from the central axis).  $B = 38$  mm

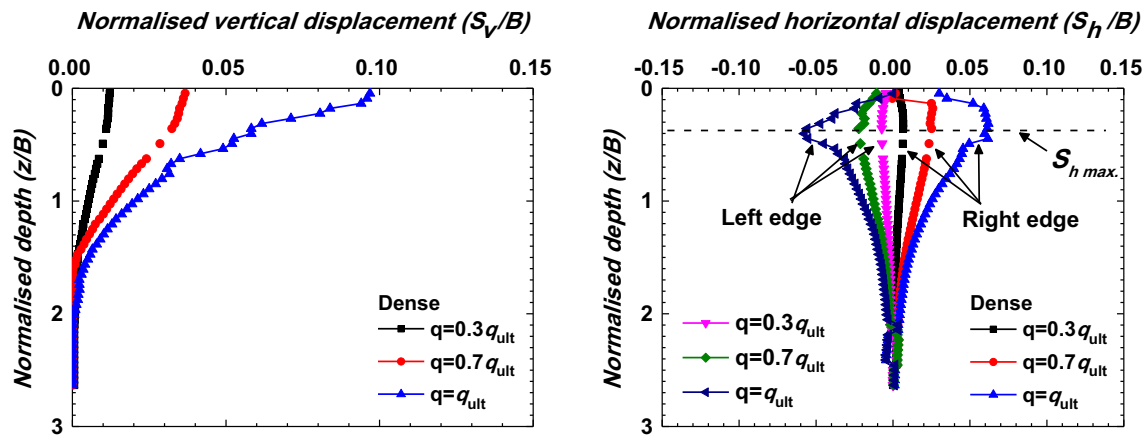


**Fig. 13** Settlement profiles with depth  $z$  from the bottom surface of the footing at different loading levels for a typical case of dense sand: (left) normalised vertical displacement component (right) normalised horizontal displacement for the sand packing.  $B = 38$  mm

The normalised vertical displacement ( $S_v/B$ ) attains the peak at a depth of about  $0.1B$  for all cases of sand packing and footing widths, which are almost independent of the loading stages.

Similarly, the normalised horizontal displacement component ( $S_h/B$ ) attains maximum at a depth of about  $0.25B$  from the surface of the footing. At  $q \leq q_{ult}$ , the maximum value of normalised vertical displacement for smaller width ( $B = 38$  mm) is:  $S_{v,max}/B = 0.070$ ,  $0.086$  and  $0.096$  and  $S_{h,max}/B = 0.02$ ,  $0.03$  and  $0.07$  for loose, medium-dense and dense sand respectively. These values increase with the relative density and load level. But, these values for the larger width of footing ( $B = 76$  mm) is:  $S_{v,max}/B = 0.045$ ,  $0.052$  and  $0.074$  for loose, medium-dense and dense sand respectively. The authors observed that the values of  $S_{v,max}/B$  at ultimate load are close to the measured values of  $S_{it}/B$  presented earlier. Interestingly, the values of  $S_{v,max}/B$  agree with the common assumption of using  $S/B$  between  $0.05B$  and  $0.1B$  for estimating  $q_{ult}$  from the load–settlement plots in foundation engineering designs [25, 36, 53]. Overall, the displacement measures reported here could be used to derive more realistic description of displacement profiles in soil media in future.

### Conclusions

PIV is shown to be effective and promising in understanding the local and global geomechanical characteristics of footing interacting with sand media of different relative densities in a coherent manner. Where possible, the displacement measures and generic characteristics of velocity fields in the sand are compared with existing literature and FEM analysis and a good level of agreement is obtained. PIV clearly shows detailed descriptions of the stages of velocity discontinuities for the sand media. The velocity

profiles of the medium-dense and dense sand are consistent with Vesic [43] but the advanced measurements reported here detect their evolutions more precisely. For the loose sand, the velocity discontinuities could reach the free surface. Significant vortex zones are existent near the footing corner at and beyond the ultimate bearing capacity of sand of all relative densities studied here. The boundaries of the zone of plastic flow in sand at failure load profiled using the advanced PIV here are remarkably similar to such intuitive diagrams suggested by the forefathers of soil mechanics, for example Fröhlich in the 1930s and Terzaghi's in 1940s [48]. The depth at which the settlement vanishes in the sand decreases for increase in the relative density of sand. The present study provides both the spatial and temporal distribution of displacements in soils of different packing densities under key stages of loading elegantly. PIV could be applied in future to develop robust failure surfaces for more complex soil profiles and foundation types encountered in geotechnical engineering applications. Further analysis is required for evaluating the scaling and size effects of footing–sand interactions in a detailed manner with a better resolution of the digital measurements (e.g. using multiple grids per grain). Also simulations using discrete element method (DEM) could be more suitable to model the grain-scale movements of granular assemblies under mechanical loading, but they would require extensive level of computing resources to study the cases considered in this work. However, as shown in the current manuscript, FEM-based displacement fields can match to the level of local-scale grain displacements of corresponding experimental systems based on PIV. In particular, experiments-based, user-defined constitutive relation was used as input in the FEM simulations here which is found to be useful. Studies are underway in our group to extend the present research strategy to account for more complex conditions and realistic sand profiles in

footing–sand interactions—for example layered soil systems, interference effects and roughness effects of footings.

## References

- Jaeger HM, Nagel SR, Behringer RP (1996) Granular solids, liquids, and gases. *Rev Mod Phys* 68(4):1259
- Duran J (2000) Sands, powders and grains. Springer, New York
- Desrues J, Viggiani G (2004) Strain localization in sand: an overview of the experimental results obtained in Grenoble using stereo photogrammetry. *Int J Num Analy Meth Geomech* 28(4):279–321
- Antony SJ (2007) Link between single-particle properties and macroscopic properties in particulate assemblies: role of structures within structures. *Philos Trans R Soc A: Math Phy Eng Sci* 365(1861):2879–2891
- Radjai F, Wolf DE, Jean M, Moreau J-J (1998) Bimodal character of stress transmission in granular packings. *Phys Rev letters* 80(1):61
- Thornton C, Antony SJ (1998) Quasi-static deformation of particulate media. *Philos Trans R Soc A Math Phys Eng Sci* 356:2763–2782
- Kruyt N, Antony SJ (2007) Force, relative-displacement, and work networks in granular materials subjected to quasistatic deformation. *Phys Rev E* 75(5):051308
- Bowles JE (1997) Foundation analysis and design, 5th edn. McGraw-Hill, Singapore
- Liu C, Evett JB (2004) Soils and foundations, 6th edn. Pearson Prentice Hall, New Jersey
- Fang H-Y (1991) Foundation engineering handbook, 2nd edn. Chapman and Hall, New York
- Das BM (2009) Shallow foundations: bearing capacity and settlement, 2nd edn. CRC Press, London
- Terzaghi K, Peck RB (1967) Soil mechanics in engineering practice. Wiley, London
- Hansbo S (1994) Foundation engineering. Elsevier, London
- Schmertmann JH, Brown PR, Hartman JP (1978) Improved strain influence factor diagrams. *J Geotech Eng Div, Proc ASCE* 104(8):1131–1135
- Powrie W (2014) Soil mechanics: concepts and applications, 3rd edn. CRC Press, London
- Mayne PW, Poulos HG (1999) Approximate displacement influence factors for elastic shallow foundations. *J Geotech Geoenviron Eng* 125(6):453–460
- Liu J, Iskander M (2004) Adaptive cross correlation for imaging displacements in soils. *J Comput Civ Eng* 18(1):46–57
- Studio Dynamic (2013) Dynamic studio user's guide. Dantec Dynamics, Skovlunde
- Albaraki S, Antony SJ (2014) How does internal angle of hoppers affect granular flow? Experimental studies using digital particle image velocimetry. *Powder Technol* 268:253–260
- Adrian RJ (1991) Particle-imaging techniques for experimental fluid mechanics. *Ann Rev Fluid Mech* 23(1):261–304
- Hamm E, Tapia F, Melo F (2011) Dynamics of shear bands in a dense granular material forced by a slowly moving rigid body. *Phys Rev E* 84(4):041304
- Murthy TG, Gnanamanickam E, Chandrasekar S (2012) Deformation field in indentation of a granular ensemble. *Phys Rev E* 85(6):061306
- Cheng Y, White DJ, Bowman ET, Bolton MD, Soga K (2001) The observation of soil microstructure under load. In: *Powders and Grains*, Balkema, pp 69–72
- White D, Take W, Bolton M (2003) Soil deformation measurement using particle image velocimetry (PIV) and photogrammetry. *Geotechnique* 53(7):619–631
- O'Loughlin C, Lehane B (2010) Nonlinear cone penetration test-based method for predicting footing settlements on sand. *J Geotech Geoenviron Eng* 136(3):409–416
- Jahanger ZK, Antony SJ, Richter J (2016) Displacement patterns beneath a rigid beam indenting on layered soil. In: *Proceedings of the 8th Americas regional conference of the international society for terrain-vehicle system*, Michigan, paper no. 67
- ASTM Standard (1989) Soil and Rock, Building, Stores, Geotextiles, 04.08, West Conshohocken, PA
- Head K (2006) Manual of soil laboratory test: soil classification and compaction tests, vol 1, 3rd edn. CRC Press, Boca Raton
- Dijkstra J, White DJ, Gaudin C (2013) Comparison of failure modes below footings on carbonate and silica sands. *Int J Phys Model Geotech* 13(1):1–12
- White D, Bolton M (2004) Displacement and strain paths during plane-strain model pile installation in sand. *Géotechnique* 54(6):375–397
- Cerato AB, Lutenegeger AJ (2007) Scale effects of shallow foundation bearing capacity on granular material. *J Geotech Geoenviron Eng* 133(10):1192–1202
- Altaee A, Fellenius BH (1994) Physical modeling in sand. *Can Geotech J* 31(3):420–431
- Lau CK (1988) Scale effects in tests on footings. PhD thesis, University of Cambridge
- Raymond GP, Komos FE (1978) Repeated load testing of a model plane strain footing. *Can Geotech J* 15(2):190–201
- Das BM (2011) Principles of foundation engineering, 7th edn. Global Engineering, Connecticut
- Kumar J, Bhoi MK (2009) Interference of two closely spaced strip footings on sand using model tests. *J Geotech Geoenviron Eng* 135(4):595–604
- ANSYS 17.2 (2016) ANSYS theory manual. ANSYS Inc, Canonsburg
- Kumar J, Kouzer K (2007) Effect of footing roughness on bearing capacity factor  $N_c$ . *J Geotech Geoenviron Eng* 133(5):502–511
- Mosadegh A, Nikraz H (2015) Bearing capacity evaluation of footing on a layered-soil using ABAQUS. *J Earth Sci Clim Change* 6(3):264
- Gordan B, Adnan A, Aida MA (2014) Soil saturated simulation in embankment during strong earthquake by effect of elasticity modulus. *Model Simul Eng* 2014:20
- Lee H-H (2015) Finite element simulations with ANSYS workbench 16. SDC Publications, USA
- Akbas SO, Kulhawy FH (2009) Axial compression of footings in cohesionless soils I: load–settlement behavior. *J Geotech Geoenviron Eng* 135(11):1562–1574
- Vesic AS (1973) Analysis of ultimate loads of shallow foundations. *J Soil Mech Found Div ASCE* 99(SM1):45–73
- De Beer EE (1965) Bearing capacity and settlement of shallow foundations on sand. In: *Proceedings of the symposium on bearing capacity and settlements of foundations*, Duke University, Durham, NC. pp 15–33
- Jewell RA (1989) Direct shear tests on sand. *Geotechnique* 39(2):309–322
- Lechinsky D, Marozzi GF (1990) Bearing capacity of shallow foundations: rigid versus flexible models. *J Geotech Eng* 116(11):1750–1756
- Selvadurai APS (1979) Elastic analysis of soil–foundation interaction. *Developments in Geotechnical Engineering*, Vol. 17, Elsevier, Amsterdam
- Terzaghi K (1943) *Theoretical soil mechanics*. Wiley, New York

49. Prandtl L (1920) Über die härte plastischer körper [On the hardness of plastic bodies]. *Math. Phys. Kl* 12:74–85 (**in German**)
50. Bolton M (1986) The strength and dilatancy of sands. *Geotechnique* 36(1):65–78
51. Lutenegeger AJ, DeGroot DJ (1995) Settlement of shallow foundations on granular soils. Report no. 6332, University of Massachusetts Transportation Centre
52. Griffiths DV, Fenton GA, Manoharan N (2006) Undrained bearing capacity of two-strip footings on spatially random soil. *Int J Geomech* 6(6):421–427
53. Lee J, Eun J, Prezzi M, Salgado R (2008) Strain influence diagrams for settlement estimation of both isolated and multiple footings in sand. *J Geotech Geoenviron Eng* 134(4):417–427